

Inclusions in calcite phantom crystals suggest role of clay minerals in dolomite formation

STEFAN FARSANG^{1,*}, PÉTER PEKKER², GIULIO I. LAMPRONTI¹, ZSOMBOR MOLNÁR²,
RASTISLAV MILOVSKÝ³, MIHÁLY PÓSEFAI², DANIEL OZDÍN⁴, TIMOTHY D. RAUB⁵, AND SIMON A.T. REDFERN^{6,†}

¹Department of Earth Sciences, University of Cambridge, Downing Street, Cambridge, CB2 3EQ, U.K.

²Research Institute of Biomolecular and Chemical Engineering, University of Pannonia, 8200 Veszprém, Egyetem u. 10, Hungary

³Earth Science Institute, Slovak Academy of Sciences, Ďumbierska 1, 974 11 Banská Bystrica, Slovak Republic

⁴Department of Mineralogy, Petrology and Economic Geology, Faculty of Natural Sciences, Comenius University, Ilkovičova 6, 842 15 Bratislava, Slovak Republic

⁵School of Earth & Environmental Sciences, University of St Andrews, Irvine Building, St Andrews, KY16 9AL, U.K.

⁶Asian School of the Environment, Nanyang Technological University, 50 Nanyang Avenue, 639798, Singapore

ABSTRACT

Micro- and nano-inclusions embedded in calcite phantom crystals from Gemerská Ves, Slovak Republic, have been characterized by a combination of Raman spectroscopy, scanning and transmission electron microscopy, X-ray powder diffraction, and C and O isotope analysis. Whereas the outer, colorless part of the phantom crystal is relatively homogeneous and cavity and inclusion-free, the inner terracotta-colored part contains abundant cavities, dolomite, hematite, goethite, titanite, phyllosilicates (mainly kaolinite and illite), and apatite inclusions and nanostructures that have formed on the walls of cavities. The nanostructures comprise hematite and goethite particles sandwiched between either two phyllosilicate crystals or a phyllosilicate and a carbonate (calcite or dolomite) crystal. Our observations suggest that all inclusions in the terracotta calcite originate from the terra rossa (a common soil type in karstic areas) and limestone outcropping adjacent to the calcite crystals. While the micrometer-sized phyllosilicate and hematite particles were likely transported from the terra rossa and attached to the surface of growing calcite, the presence of phyllosilicates that are only a few atomic layers thick and of euhedral hematite, goethite, and dolomite crystals suggests that these particles precipitated along with the phantom calcite in situ, from an aqueous solution carrying terra rossa-derived and limestone-derived solutes. The compositional differences between the terra rossa (e.g., smectite as the only major Mg-rich phase) and terracotta calcite inclusions (e.g., dolomite as the only major Mg-rich phase and the presence of only Mg-free clays) hint that a smectite-illite conversion provides the Mg necessary for the precipitation of dolomite and possibly the Fe associated with the iron oxyhydroxide nanostructures. Phyllosilicate nucleation on calcite and dolomite nucleation on phyllosilicates, as inferred from nanoscale mineralogical associations, suggest that carbonates and phyllosilicates may mutually enhance nucleation and growth. This enhancement may result in the formation of large-scale clay-carbonate successions in aqueous settings, including the enigmatic, pink-colored cap dolostones succeeding late Neoproterozoic “Snowball Earth” deposits. The distribution of inclusions in the terracotta calcite and the preferred nucleation of hematite and goethite on phyllosilicate, rather than on carbonate surfaces, indicates that phyllosilicates have a potential to not only disrupt crystal growth and trigger the formation of cavities in the structure of the calcite host, but also to provide surfaces for the precipitation of different phases in the cavities and to uniformly distribute otherwise incompatible materials in a calcite host crystal. This calls for further exploration of the potential application of phyllosilicates in composite structure development.

Keywords: Calcite, cap carbonate, clay, dolomite, hematite, goethite, illite, kaolinite, nanoparticle, nucleation, phantom crystal, phyllosilicate, Raman spectroscopy, SEM, Snowball Earth, TEM, XRD

INTRODUCTION

A phantom crystal is a crystal embedded in another crystal of the same mineral species with visible outlines. The embedded crystal is visible due to some variation in composition (e.g., substitution of atoms, presence of inclusions) or the attachment of

particles to its surface. Examples include: quartz (SiO₂) phantom crystals outlined by green chlorite from Comechas em Cima, Serra do Cabral, Minas Gerais, Brazil; by green fuchsite from Ihovitra, Ambatofinandrahna, Madagascar; by white clay minerals from Santo Antonio mine, Serra do Cabral, Minas Gerais, Brazil; by black manganese minerals from Alegre mine, near Mimoso, Bahia, Brazil, and calcite (CaCO₃) phantom crystals outlined by pyrite from Korsnas mine, Finland, and the Surneshko Kladenche copper vein deposit, Rossen Ore Field, Bulgaria; and

* E-mail: sf571@cam.ac.uk. Orcid 0000-0002-4918-5566

† Orcid 0000-0001-9513-0147

by dark red hematite from Chihuahua state, Mexico (Johnston and Butler 1946; Sinkankas 1966; Rehtijärvi and Kinnunen 1979; Gornitz 1981; Bonev et al. 2005; Farfan and Post 2019). In the latter, the pre-existing calcite crystals are scalenohedra coated with dark red hematite (Fe_2O_3), which are overgrown by transparent rhombohedra (Sinkankas 1966; Gornitz 1981). Calcite phantom crystals originating from Gemerská Ves, Slovakia, have a distinct terracotta color (Fig. 1) and display a range of crystal forms, the most abundant being scalenohedra, hexagonal prisms, and rhombohedra, while these forms are usually shared by the embedded and embedding crystals (Bálintová et al. 2006). Here, we characterize inclusions of these calcite phantom crystals by size, distribution, and mineralogy and propose a formation scenario for the phantom crystals.

METHODS

Raman spectroscopy

A confocal LabRAM 300 (Horiba Jobin Yvon) Raman spectrometer with 300 mm focal length objective, at the Department of Earth Sciences, University of Cambridge, was used to collect Raman spectra from 100 to 1800 cm^{-1} . A holographic grating of $1800\text{ gr}\cdot\text{mm}^{-1}$ coupled to a Peltier front-illuminated CCD detector (1024×256 pixel in size) enabled a spectral resolution of $\sim 1\text{ cm}^{-1}$. The excitation line at 532.05 nm was produced by a Ventus 532 laser source (Laser Quantum) focused on the sample using an Olympus LMPLFLN $50\times$ long working distance objective.

All Raman spectra were treated using PeakFit software. For each Raman spectrum, the baseline was subtracted, and peak features were determined by least squares fitting to Voigt profiles for each Raman band. Peak positions were calibrated against the measured excitation of a Ne light emission reference spectrum (Saloman and Sansonetti 2004).



FIGURE 1. Phantom calcite from Gemerská Ves, Slovakia. (Color online.)

Scanning electron microscopy (SEM)

For SEM analysis, a phantom calcite sample mounted in epoxy was polished with colloidal silica, carbon-coated, and analyzed under high vacuum conditions. A FEI Quanta 650 F instrument equipped with two Bruker XFlash 630 silicon drift EDX detectors at the Department of Earth Sciences, University of Cambridge, was employed for backscattered electron (BSE) imaging and for qualitative chemical analysis by energy-dispersive spectroscopy (EDS). An accelerating voltage of 15 keV , beam spot size of 4.5 , and a working distance of 13 mm was used.

To investigate the mineralogical makeup of terra rossa, it was powdered and deposited on amorphous carbon support film. An FEI Apreo LoVac instrument equipped with an EDAX METEK Octane Elect Plus EDX detector at the Department of Material Sciences, University of Pannonia, was employed for BSE imaging and for qualitative chemical analysis by EDS. An accelerating voltage of 20 keV , beam spot size of 4.5 , and a working distance of 10 mm was used.

Transmission electron microscopy (TEM)

Two samples were prepared for TEM analysis. The first was prepared by depositing a drop of aqueous suspension of the ground particles of the terracotta-colored calcite onto a 200 mesh copper TEM grid covered by a lacey carbon amorphous support film. The second sample was a section of terracotta-colored calcite cut perpendicular to the growth lines and mounted in a 3 mm Cu support ring. The sample was thinned to $50\text{ }\mu\text{m}$ and then ion milled.

TEM analyses were performed using a Talos F200X G2 instrument (Thermo-Fisher Scientific) at the Nanolab, University of Pannonia. The instrument is equipped with a field-emission gun, a Ceta 16M camera, and a four-detector Super-X energy-dispersive X-ray spectrometer and is capable of working in both conventional TEM and scanning transmission (STEM) modes. The instrument was operated at 200 kV accelerating voltage. Low-magnification bright-field (BF) images, high-resolution (HRTEM) images, and selected-area electron diffraction (SAED) patterns were obtained in TEM mode. STEM high-angle annular dark-field (HAADF) images were collected both for high-resolution structure analyses and for mapping elemental compositions by coupling STEM imaging with energy-dispersive X-ray spectrometry (EDS).

X-ray powder diffraction (XRD)

XRD was conducted at the Department of Earth Sciences, University of Cambridge. Powder diffraction data of breccia were collected from 10 to $60^\circ 2\theta$ (0.02° step size) in Bragg-Brentano geometry on a D8 Advance Bruker powder diffractometer using $\text{MoK}\alpha$ X-rays and a LYNXEYE XE-T position sensitive detector. Powder diffraction data of terra rossa were collected from 4 to $50^\circ 2\theta$ (0.04° step size) in Bragg-Brentano geometry on a D8 Advance Bruker powder diffractometer using $\text{CuK}\alpha$ radiation and a Vantec position sensitive detector.

Rietveld refinements were performed using TOPAS-Academic V6 (Coelho 2018). Starting crystal structures of all mineral phases were retrieved from the Inorganic Crystal Structure Database (Allmann and Hinek 2007). Instrumental parameters were modeled by refining data collected from a LaB_6 660b NIST standard. A shifted Chebyshev function with eight parameters was used to fit the background. The peak shape was modeled using a pseudo-Voigt function. The March-Dollase model was used to correct for preferred orientation on the following crystallographic planes: (104) for calcite; (001) for kaolinite, illite, and montmorillonite; and (100) for goethite. The refinement converged to a final χ^2 and R_p of 6.73 and 16.04% , respectively, for the breccia, and 2.04 and 2.49% , respectively, for the terra rossa.

C and O isotopes

C and O stable isotope ratios were measured using a Gasbench III preparation device coupled to isotope-ratio mass-spectrometer MAT 253 (both Thermo-Fisher Scientific). Microdrilled samples of calcite (60 – $80\text{ }\mu\text{g}$) were loaded into 5 mL borosilicate glass vials (Labco), sealed by caps with rubber septa, and flushed with helium to remove atmosphere. Subsequent phosphoric acid digestion (McCrea 1950) took place at 40°C overnight. The evolved CO_2 gas was analyzed in continuous-flow mode in helium as carrier gas. In each run, three reference gas peaks were followed by four pulses of sample CO_2 . Raw isotope ratios were calibrated using an international reference material NBS-18 with $\delta^{13}\text{C} = +5.014\text{‰}$, $\delta^{18}\text{O} = -23.2\text{‰}$ and two working standards with $\delta^{13}\text{C} = +2.48\text{‰}$, $\delta^{18}\text{O} = -2.40\text{‰}$ and $\delta^{13}\text{C} = -9.30\text{‰}$, $\delta^{18}\text{O} = -15.30\text{‰}$, respectively. Typical precision of measurements is 0.1‰ for C and 0.2‰ for O (1σ). Isotope values are reported as permil with reference to the international standard Vienna Pee Dee Belemnite (VPDB).

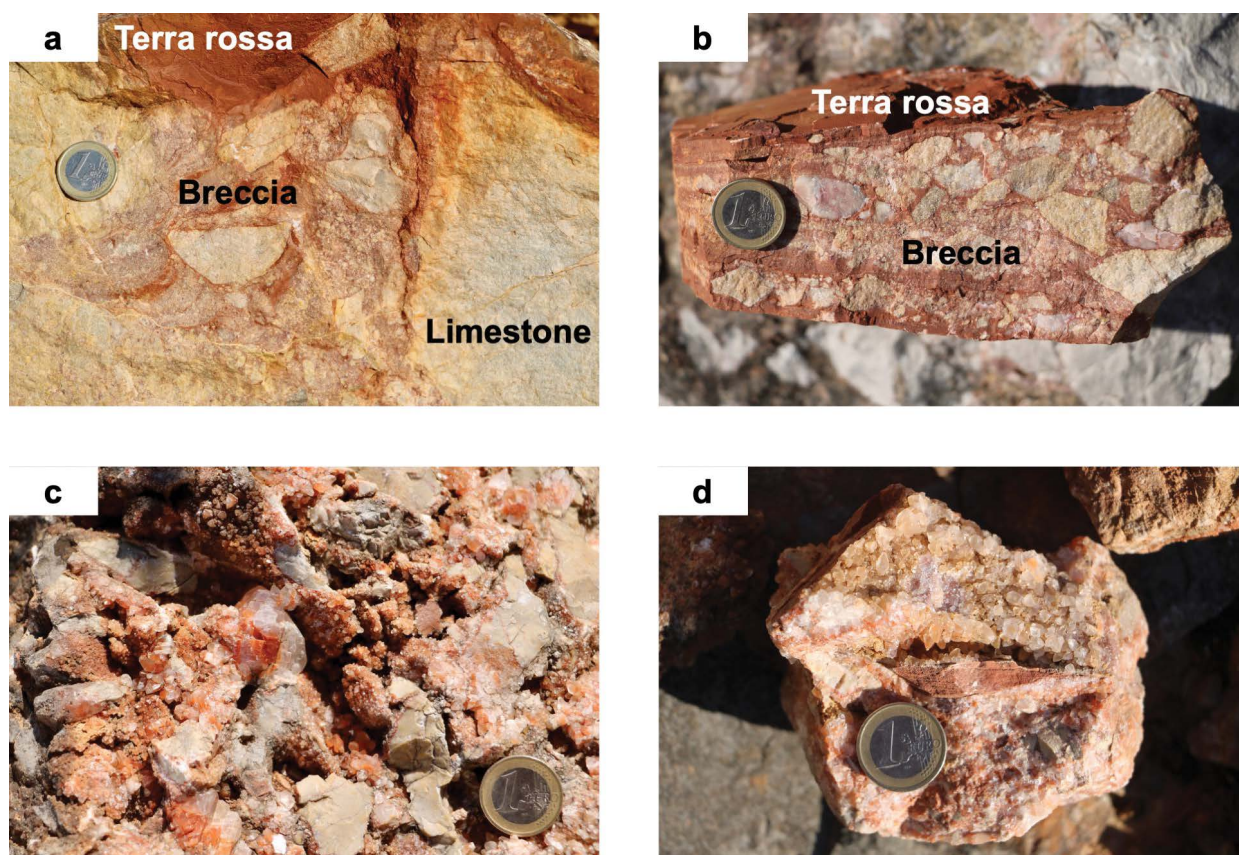


FIGURE 2. Rocks of the outcrop: (a) limestone–breccia contact. The breccia contains limestone clasts and terra rossa rich layers, (b) sample of breccia coming from the edge of the body, (c) the center of the body with vugs and (d) sample of breccia coming from the center of the body. The coin for scale has a diameter of 23.25 mm. (Color online.)

RESULTS AND DISCUSSION

Mineralogy

The phantom calcite was sampled at N 48° 29.147' E 20° 15.112' in a quarry west of Gemerská Ves village, Revúca county, Banská Bystrica region, Slovakia. The quarry is an outcrop of Middle Triassic Wetterstein limestone (Elečko et al. 1985) with colorless and whitish calcite crystals commonly occurring in its vugs. The massive limestone body is cut by an elongated body of red breccia, up to 5 m wide running NE-SW, that contains centimeter-sized limestone clasts in a fine-grained, layered matrix composed of terra rossa (a common soil type in karstic areas) and calcium carbonate (Fig. 2). Such rocks are abundant in the region (Slovak karst) and may form by the collapse of cave walls and ceilings (e.g., karst collapse breccia) or can be related to faults in karstic areas (e.g., footwall breccia) (Gaal 2008). Near the limestone–breccia contact, the breccia is consolidated and does not contain euhedral calcite crystals (Figs. 2a and 2b). In contrast, the central part of the breccia body is rich in vugs that contain calcite crystals up to 10 cm in size (Figs. 2c and 2d). Calcite crystals growing close (a few millimeters) to the terra rossa typically contain a terracotta-colored inner part, while those sitting further away are colorless or whitish without an embedded terracotta crystal (Fig. 2d).

The Raman spectrum of calcite has six peaks corresponding to five Raman-active vibrational modes (translational external E_g , librational external E_g , internal $\nu_4 E_g$, internal $\nu_1 A_{1g}$, and internal $\nu_3 E_g$) and an overtone mode, which represents the $2\nu_2$ overtone mode of the IR-active $\nu_2 A_{2u}$ mode (Krishnan 1945; Couture 1947; Krishnamurti 1957; De La Pierre et al. 2014). The spectrum of our reference material, a natural calcite crystal from Miskolctapolca, Hungary, shows features corresponding to these vibrational modes at 158, 284, 713, 1088, 1438, and 1751 cm^{-1} , respectively (Farsang et al. 2018). These six peaks are detected in both the colorless and terracotta-colored parts of calcite (Figs. 3a–3d). The satellite peaks detected at 1067 and 1066 cm^{-1} in the colorless and terracotta-colored parts, respectively, are assigned to isotopic substitutions of ^{13}C and ^{18}O (Cloots 1991).

Hematite possesses seven Raman-active vibrational modes (A_{1g} , E_g , E_g , E_g , E_g , A_{1g} , and E_g), and its Raman spectrum also exhibits the highest-frequency $2E_u$ overtone mode (Beattie and Gilson 1970; Massey et al. 1990; Shim and Duffy 2002). The spectrum of our reference material, a natural hematite crystal from Elba, Tuscany, Italy (Sedgwick Museum of Earth Sciences, University of Cambridge specimen number 822), shows frequency features corresponding to the aforementioned vibrational modes at 224, 243, 290, 294, 404, 497, 604, and 1305 cm^{-1}

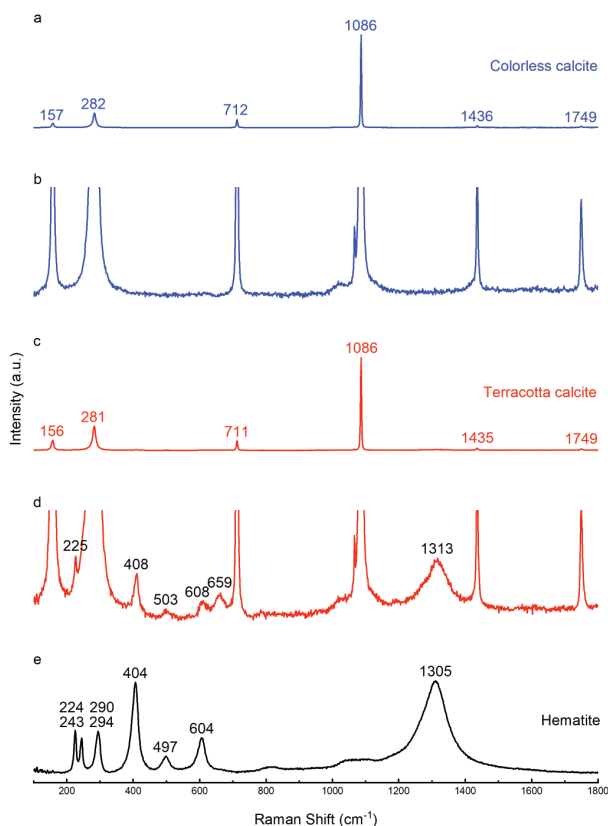


FIGURE 3. Raman spectra of (a–b) colorless part of calcite, (c–d) terracotta part of calcite, and (e) hematite. (b and d) The absence and presence of low-intensity features in a and c, respectively, are shown. (Color online.)

(Fig. 3e). In the spectrum of terracotta-colored calcite, there are clearly visible bands at 225, 408, 503, 608, and 1313 cm^{-1} , while those expected around 243, 290, and 294 cm^{-1} are hidden by the strong signal produced by calcite (Fig. 3d). In the same spectrum, there is an additional prominent peak at 659 cm^{-1} . This has only been observed in studies in which the complete symmetry of the hematite structure is lowered either due to partial substitution of Fe atoms, as demonstrated in the case of $\text{Fe}_x\text{Cr}_{2-x}\text{O}_3$ ($0 \leq x \leq 2$) solid solution, or by defects induced by stress (McCarty and Boehme 1989; Shim and Duffy 2002). In our case, the very small size of hematite particles (see below) with a significant proportion of atoms located at or near their surface may lead to the lowering of symmetry, giving rise to the peak at 659 cm^{-1} .

Scanning electron microscopy shows that while the colorless part of the crystal is a relatively homogeneous and cavity and inclusion-free calcite, the terracotta-colored part contains abundant cavities and inclusions of different types, concentrated along growth lines, possibly resulting from episodic calcite growth (Figs. 4a–4b). The cavities have irregular shapes and range from submicrometer to several tens of micrometers in size. The largest inclusions are dolomite (Figs. 4c–4d), phyllosilicate (Fig. 4e), and apatite (Figs. 4e–4f) particles with sizes ranging up to ~ 50 μm . Smaller inclusions include abundant hematite and rare rutile particles with sizes up to ~ 5 μm . The dolomite is richer in inclu-

sions than its calcite host and can show an intimate relationship with calcite (Fig. 4c) or occur as euhedral crystals (Fig. 4d). EDS reveals the presence of two types of phyllosilicate: an Al- and Si-rich phase (likely kaolinite) and one with additional K (probably illite). The SEM observations are consistent with electron probe microanalysis data of Bálintová et al. (2006) that show slightly elevated levels of MgO, FeO, and MnO in the terracotta-colored part (0.26, 0.04, and 0.02 wt%, respectively, compared to 0.22, 0.01, and 0.01 wt%, in the colorless part).

Sub-micrometer textural analysis by transmission electron microscopy reveals high abundance and fine-scale distribution of cavities in the terracotta calcite. The walls of these cavities are covered by phyllosilicates, often only a few atomic layers thick, to which submicrometer and nanosized tabular hematite particles are generally attached (Figs. 5a–5c and 6a–6b). This explains the presence of bands corresponding to hematite in the Raman spectra from the terracotta part, even when no particles are visible by optical microscopy. Apart from the phyllosilicate-hematite-carbonate sandwich structures, phyllosilicate-hematite-phyllosilicate structures also commonly occur. TEM also reveals the presence of tabular goethite that, just like hematite, is either sandwiched between two phyllosilicate crystals or between a phyllosilicate and a carbonate crystal (Figs. 6c–6d). The clearly visible T-O-T sequence of layers, the ~ 10 Å spacing of these layers (Figs. 5c and 6c), and the high-K concentration detected by EDS suggest that at least some of the phyllosilicate is illite. A very similar association, with nanosized hematite particles sandwiched between illite, has been found in claystone from Mecsek Mountains, Hungary, and seems to be a common nanostructure in Fe and clay-rich environments (Németh et al. 2016). In calcite cavities containing dolomite, the walls of cavities (i.e., the space in between the host calcite and dolomite inclusion) are also covered by phyllosilicate crystals (Figs. 4c–4d), suggesting dolomite nucleation and growth may take place on phyllosilicate surfaces. The distinct color of terracotta calcite is likely the result of light scattering produced by the three main mineral phases/groups of inclusions: dark red hematite and whitish dolomite and phyllosilicates.

To identify the potential source of particles in the terracotta calcite, the mineralogy of the breccia and terra rossa surrounding the calcite crystals was also analyzed. X-ray powder diffraction (XRD) of the breccia reveals the presence of calcite and hematite (Fig. 7a). In the adjacent terra rossa, XRD data indicate the presence of phases consistent with kaolinite, illite, montmorillonite, and goethite (Fig. 7b). In addition to clay minerals, SEM EDS analyses detect hematite, apatite, and titanite in the terra rossa. The two major differences between the composition of the terra rossa and the inclusions of terracotta calcite are: (1) the presence of Mg-rich phyllosilicates in the terra rossa and their absence in the terracotta calcite, and (2) the lack of dolomite in the terra rossa and its presence in the terracotta calcite. An explanation for these differences is provided in the Paragenesis section text. Nevertheless, the terra rossa containing breccia is the likely source of inclusions in the phantom calcite.

C and O isotopes

A single sample containing a limestone clast, terracotta calcite, and colorless calcite adjacent to one another was chosen for C and O isotope analysis (Online Materials! Fig. OM1).

All three parts show distinct C and O isotope compositions (Fig. 8 and Online Materials¹ Table OM1). The limestone has $\delta^{13}\text{C}$ values of $\sim 0\text{‰}$ and $\delta^{18}\text{O}$ values of $\sim -6\text{‰}$, similar to other Triassic limestones found in the Carpathian region (Haas et al. 2006). The terracotta calcite has $\delta^{13}\text{C}$ ranging from -1 to -2‰ , and $\delta^{18}\text{O}$ ranging from -12 to -15‰ , whereas the colorless calcite has $\delta^{13}\text{C}$ of $\sim -3.5\text{‰}$ and $\delta^{18}\text{O}$ of $\sim -8\text{‰}$, indicating significant differences in the composition and/or temperature of fluid from which the terracotta calcite and colorless calcite precipitated.

Paragenesis

Based on the distinct mineralogy and isotope composition of the terracotta-colored and colorless parts of calcite, we propose that these two parts precipitated from two distinct fluids. First, the terracotta-colored crystals formed from a fluid that likely carried (1) limestone-derived solutes; (2) terra rossa-derived minerals, i.e., micrometer-sized refractory particles of the terra rossa outcropping in the breccia body adjacent to the limestone (e.g., phyllosilicates, hematite); and (3) terra rossa-derived solutes.

As the calcite crystals grew, micrometer-sized terra rossa-

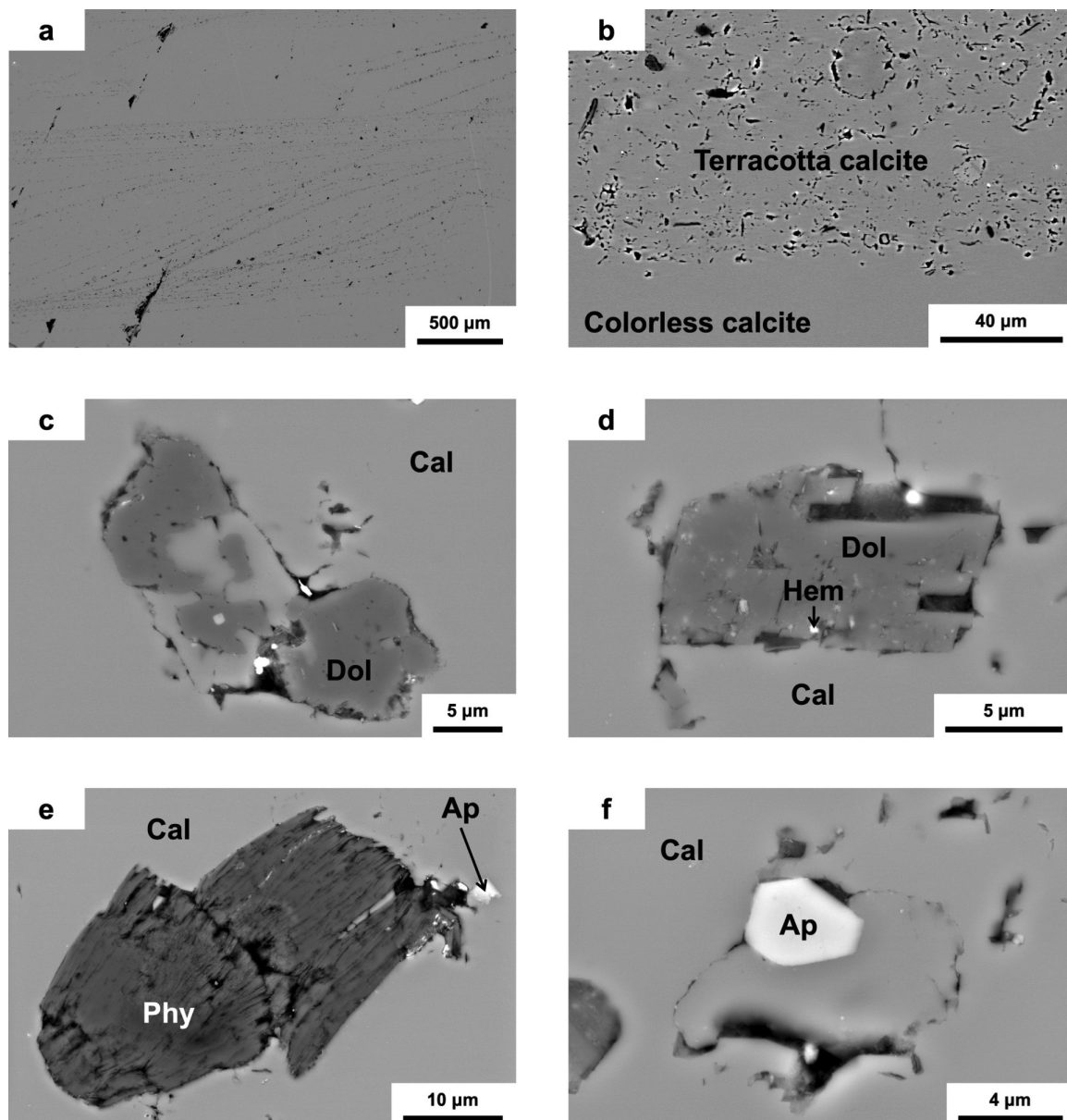


FIGURE 4. (a) cavity- and particle-rich zones in terracotta calcite, (b) boundary between the colorless, cavity- and particle-free calcite and the terracotta-colored, cavity- and particle-rich calcite, (c–f) particles in the terracotta-colored calcite: (c and d) dolomite, (e) phyllosilicate, and (f) apatite. Ap = apatite; Cal = calcite; Dol = dolomite; Hem = hematite; Phy = phyllosilicate. BSE images.

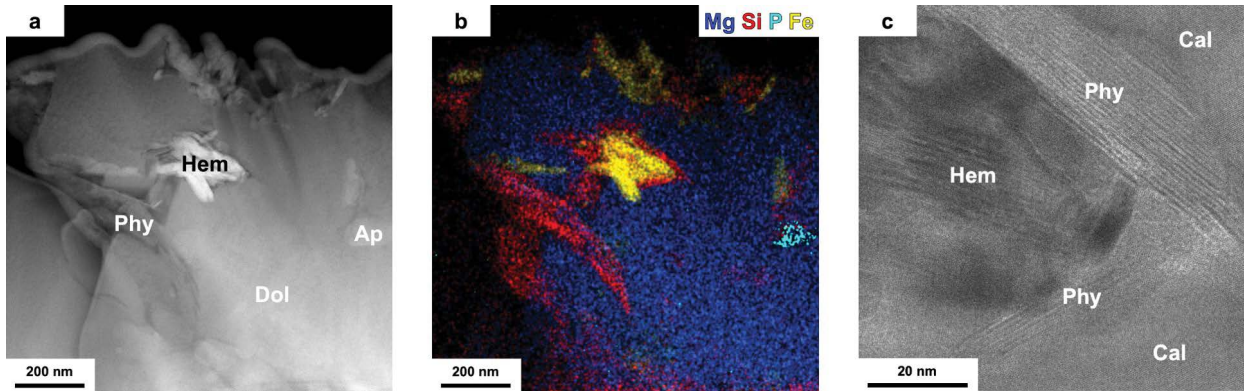


FIGURE 5. (a) STEM HAADF image and (b) combined EDS element map of a hematite-rich region. High concentrations of Mg correspond to dolomite, Si to phyllosilicate, P to apatite, and Fe to hematite. (c) HRTEM image showing the intimate relationship between calcite, phyllosilicates, and hematite. Ap = apatite; Cal = calcite; Dol = dolomite; Hem = hematite; Phy = phyllosilicate. (Color online.)

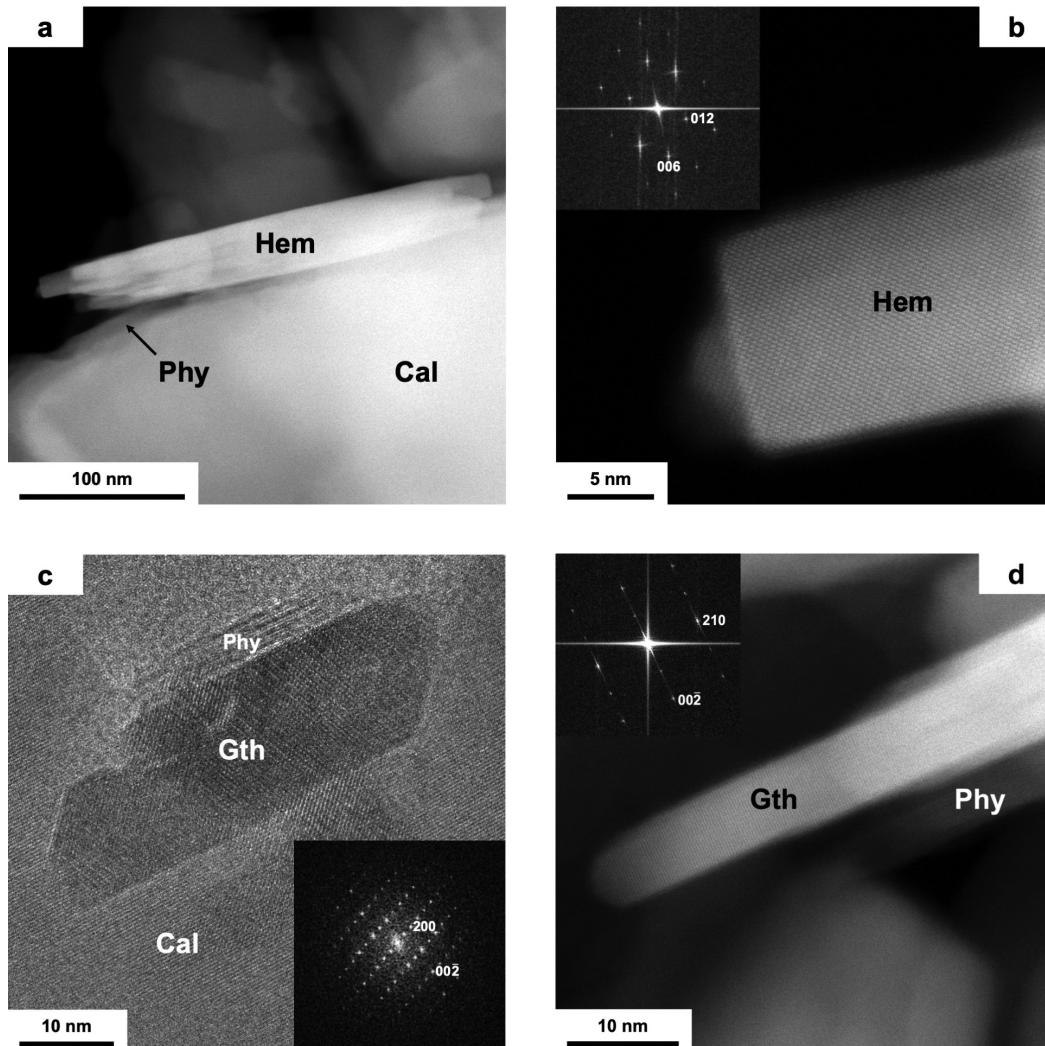


FIGURE 6. (a) STEM HAADF image and (b) HR STEM HAADF image of hematite and its Fourier transform (FT) image with Miller indices indicated. The hematite grows on a phyllosilicate attached to the walls of a cavity in calcite. (c) HRTEM image of goethite with phyllosilicate and calcite and the FT image of the goethite with Miller indices indicated. (d) HR STEM HAADF image of goethite with phyllosilicate and the FT image of the goethite with Miller indices indicated. Cal = calcite; Gth = goethite; Hem = hematite; Phy = phyllosilicate.

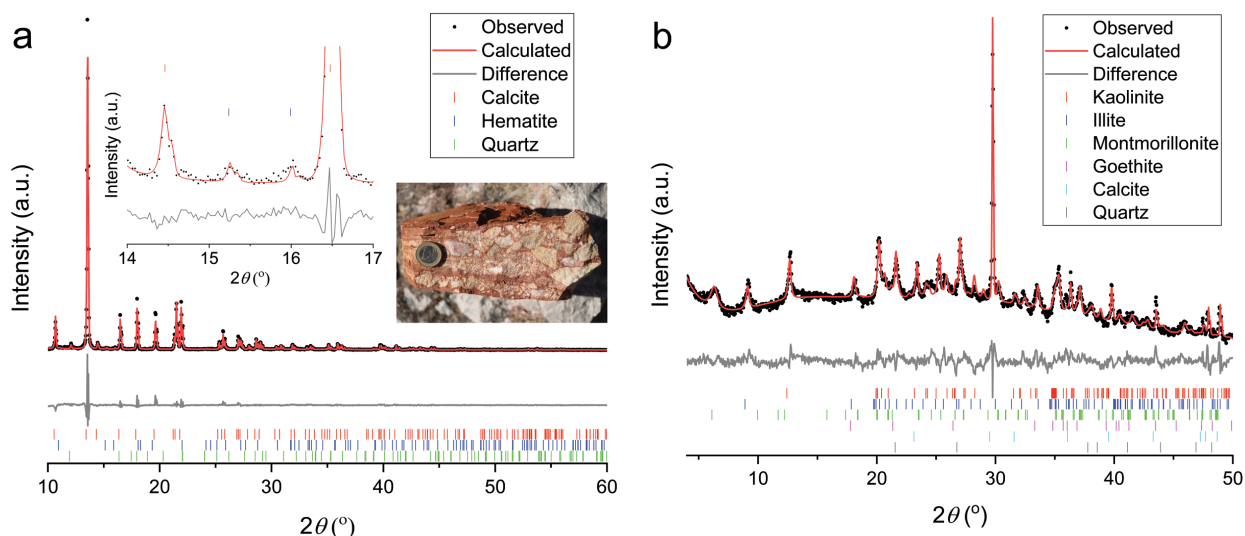


FIGURE 7. XRD pattern of phases in (a) breccia: calcite, hematite, and quartz; and (b) terra rossa: kaolinite, illite, montmorillonite, goethite, and quartz. Quartz is most likely contamination. (Color online.)

derived mineral particles likely attached to the surfaces of growing calcite crystals, creating zones in the host calcite. In addition, a range of nanoparticles likely coprecipitated in situ on the surfaces of growing calcite crystals from terra rossa-derived solutes, including phyllosilicates, often only a few atomic layers thick. This was most probably followed by the precipitation of Fe-oxyhydroxides or dolomite on phyllosilicate nanoparticles. Here we acknowledge the ambiguity associated with discerning the origin (transport vs. in situ precipitation) of the phases contained within both the terracotta calcite and the parent material (e.g., hematite) based on crystal size and/or morphology alone. It is possible that the larger, micrometer-sized particles also precipitated in situ from terra rossa-derived solutes or that the smaller nanoparticles were also transported from the terra rossa.

Preferential attachment of Fe-oxyhydroxide particles to phyllosilicate nanoparticles rather than to the calcite matrix is likely due to the heterogeneously charged surfaces of clays (Tombácz and Szekeres 2006). Intimate association of magnetite nanoparticles with phyllosilicates in physical magnetic separations of marls is commonly documented in the paleomagnetic literature (e.g., Montgomery et al. 1998). A reaction mechanism by which ferric iron is sourced from larger, physically deposited clays, as opposed to electrostatic attachment onto the smaller, neofomed phyllosilicates, also is plausible as described below.

Dolomite likely grew simultaneously with the host calcite, while the fluid was still Mg-rich due to the terra rossa-derived solutes. We note that dolomite inclusions are the only Mg-bearing particles in the terracotta calcite, while Mg-rich phyllosilicates present in the terra rossa are absent from the terracotta calcite. Instead, Mg-free phyllosilicates (kaolinite and illite) are present, further supporting the idea that Mg leached from Mg-rich phyllosilicates led to the formation of dolomite. Indeed, a smectite-illite conversion has been invoked previously as the possible source of ions that form dolomites (McHargue and Price 1982), and we believe that here the same process takes place.

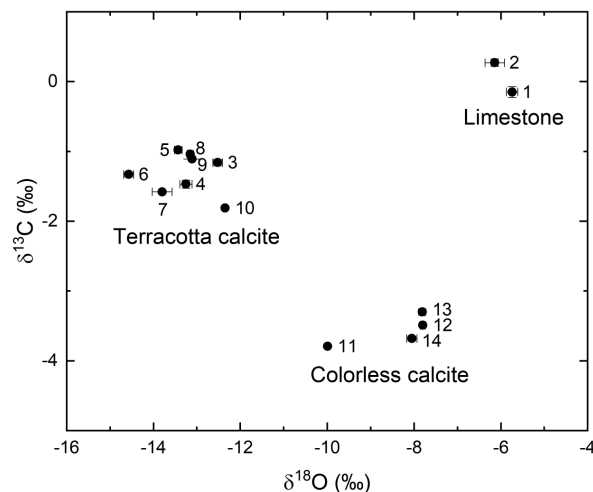


FIGURE 8. C and O isotope data. The numbers next to data points correspond to points of analysis in Online Materials¹ Figure OM1.

The smectite-illite conversion has previously been associated with neofomation of iron oxide nanocrystals (Katz et al. 1998, 2000; Woods 2002) as ferrous and ferric iron substitute in the tetrahedral and octahedral phyllosilicate sites, respectively. Although magnetite is commonly observed as the clay paragenetic iron oxide product, most studies of the magnetic effect of the transition have concerned carbonaceous mudstones near reduced-fluid (volcanic) heat sources (cf. also Eslinger et al. 1979); so in an oxic setting such as terra rossa limestone breccia vugs hosting terracotta calcite, ferric oxyhydroxides are presumably viable phyllosilicate-conversion products (Hyodo et al. 2020). It is unlikely that smectite-illite conversion is occurring in the smallest (several atomic layers thick) phyllosilicates, which are neofomed from solution as described above. Larger smectites physically transported from terra rossa limestone, however,

plausibly liberated ferric iron to solution during conversion to illite in the hydrothermal fluid, so larger hematite and goethite crystals may be neoformed by that mechanism. We note that the low, negative oxygen isotope values of terracotta calcite are consistent with this elevated temperature, which promotes the smectite-illite conversion.

The formation of terracotta-colored crystals was likely followed by the precipitation of colorless part of crystals from a fluid that only contained limestone-derived solutes. The lack of dolomite particles in the colorless part provides further support for Mg originating from the terra rossa. These lower-temperature fluids, with an intermediate oxygen isotopic composition between that of marine limestone and hydrothermal terracotta calcite, were likely distributed along fractures or faults associated with the formation of the breccia body. Their lower, more negative carbon isotope values compared to terracotta calcite is consistent with precipitation from a distilled residual fluid.

IMPLICATIONS

It has been suggested previously that phyllosilicates (e.g., smectites) promote the nucleation and growth of Ca-Mg carbonate minerals (Nyirő-Kósa et al. 2018; Fodor et al. 2020). Phyllosilicate nucleation on calcite and dolomite nucleation on phyllosilicates, as inferred from nanoscale mineralogical associations, suggest that carbonates can also provide surfaces for the growth of phyllosilicates, and this mutual enhancement may result in the formation of large-scale clay-carbonate successions in aqueous settings. Indeed, primary dolostones are rich in Mg-rich phyllosilicates (Weber 1964; Raub et al. 2007; Bristow et al. 2011), which were proposed to play a crucial role in primary dolomite formation in a diverse set of environments, including the seafloor (Kahle 1965), lakes (Wanas and Sallam 2016), and soils (Díaz-Hernández et al. 2013; Cuadros et al. 2016). Post-Snowball Earth cap dolostones, intriguingly, are terracotta-colored and contain abundant hematite, maghemite, and oxidized magnetite carrying primary magnetization and associated with ubiquitous phyllosilicates (Raub et al. 2007).

Our results show that dolomite precipitation is also possible in karstic environments where limestone is in contact with soil (terra rossa), from fluids dissolving Ca-carbonate and simultaneously leaching Mg from phyllosilicates. Recently, Mg-bearing calcium carbonate and dolomite formation at ambient conditions in the presence of clays has been shown experimentally (Liu et al. 2019; Molnár et al. 2021).

The mineralogy of inclusions in the terracotta calcite can suggest leads for the development and design of composite structures, which has been long recognized as one of the key approaches of making new functional materials with tailored properties (Ramamurthy and Eaton 1994). Calcite, being one of the most abundant and important industrial materials and biominerals, has received a great deal of attention within the materials science and engineering community.

A wide range of organic and inorganic materials have been incorporated into the calcite structure to control its optical, mechanical, and magnetic properties (e.g., Kim et al. 2011; Kulak et al. 2014; Rae Cho et al. 2016; Green et al. 2016). The latter, for instance, has been achieved by the occlusion of magnetite (Fe₃O₄) nanoparticles into a calcite single-crystal

matrix using a copolymer to control the homogeneous distribution of magnetite particles while limiting their aggregation and migration (Kulak et al. 2014). The distribution of inclusions in the terracotta calcite and the preferred nucleation of hematite and goethite on phyllosilicate rather than carbonate surfaces indicates that phyllosilicates have a potential to not only disrupt crystal growth and trigger the formation of cavities in the structure of the calcite host but also to provide a surface for the precipitation of different phases in the cavities and to uniformly distribute otherwise incompatible materials in the calcite host crystal. Indeed, the attachment of other oxides, including magnetite and TiO₂ nanoparticles, to phyllosilicates has been observed previously (Galindo-Gonzalez et al. 2009; Zhou et al. 2012; Cai et al. 2014), and the potential application of phyllosilicates in composite structure development should therefore be further explored.

ACKNOWLEDGMENTS

We thank Stefan Farsang Sr. for his help with sample collection. The Sedgwick Museum of Earth Sciences, University of Cambridge, is acknowledged for the hematite sample. We thank Tamás G. Weiszborg for a constructive discussion as well as the anonymous reviewers and the associate editor Adam Wallace for their helpful comments and suggestions.

FUNDING

This work was supported by the Natural Environment Research Council (grant number NE/L002507/1) and the Slovak Research and Development Agency (grant number APVV-19-0065). TEM studies were performed at the electron microscopy laboratory of the University of Pannonia, established using grant number GINOP-2.3.3-15-2016-0009 from the European Structural and Investments Funds and the Hungarian Government.

REFERENCES CITED

- Allmann, R., and Hinek, R. (2007) The introduction of structure types into the Inorganic Crystal Structure Database ICSD. *Acta Crystallographica*, A63, 412–417.
- Bálintová, T., Ozdín, D., Fejdi, P., Števkó, M., Gregor, M., and Stankovič, J. (2006) Mineralogické štúdium fantómových kalcitov z Gemerskej Vsi—Mineralogical study of phantom calcite from village Gemerská Ves, Slovakia. *Mineralia Slovaca*, 38, 124–130 (in Slovak).
- Beattie, I.R., and Gilson, T.R. (1970) The single-crystal Raman spectra of nearly opaque materials. Iron(III) oxide and chromium(III) oxide. *Journal of the Chemical Society A: Inorganic, Physical, Theoretical*, 980–986.
- Bonev, I.K., Garcia-Ruiz, J.M., Atanassova, R., Otalora, F., and Petrusenko, S. (2005) Genesis of filamentary pyrite associated with calcite crystals. *European Journal of Mineralogy*, 17, 905–913.
- Bristow, T.F., Bonifacie, M., Derkowski, A., Eiler, J.M., and Grotzinger, J.P. (2011) A hydrothermal origin for isotopically anomalous cap dolostone cements from south China. *Nature*, 474, 68–71.
- Cai, L., Tong, M., Wang, X., and Kim, H. (2014) Influence of clay particles on the transport and retention of titanium dioxide nanoparticles in quartz sand. *Environmental Science & Technology*, 48, 7323–7332.
- Cloots, R. (1991) Raman spectrum of carbonates M^{II}CO₃ in the 1100–1000 cm⁻¹ region: Observation of the n₁ mode of the isotopic (C¹⁶O₂¹⁸O)²⁻ ion. *Spectrochimica Acta Part A: Molecular Spectroscopy*, 47, 1745–1750.
- Coelho, A.A. (2018) TOPAS and TOPAS-Academic: an optimization program integrating computer algebra and crystallographic objects written in C++. *Journal of Applied Crystallography*, 51, 210–218.
- Couture, L. (1947) Étude des spectres de vibrations de monocristaux ioniques. *Annales de Physique*, 12, 5–94. EDP Sciences.
- Cuadros, J., Diaz-Hernandez, J.L., Sanchez-Navas, A., Garcia-Casco, A., and Yepes, J. (2016) Chemical and textural controls on the formation of sepiolite, palygorskite and dolomite in volcanic soils. *Geoderma*, 271, 99–114.
- De La Pierre, M., Carteret, C., Maschio, L., André, E., Orlando, R., and Dovesi, R. (2014) The Raman spectrum of CaCO₃ polymorphs calcite and aragonite: A combined experimental and computational study. *The Journal of Chemical Physics*, 140, 164509.
- Díaz-Hernández, J.L., Sánchez-Navas, A., and Reyes, E. (2013) Isotopic evidence for dolomite formation in soils. *Chemical Geology*, 347, 20–33.
- Elečko, M., Gaál, E., Lexa, J., Mello, J., Prištaš, J., Vass, D., and Vozárová, A. (1985) Geologická mapa Rimavskej kotliny a príľahlej časti Slovenského rudohoria 1:50 000—Geological map of the Rimava Basin and the adjacent part of the Slovak Ore Mountains 1:50 000 (in Slovak). Bratislava. GÚDS.
- Eslinger, E., Highsmith, P., Albers, D., and De Mayo, B. (1979) Role of iron reduc-

- tion in the conversion of smectite to illite in bentonites in the disturbed belt, Montana. *Clays and Clay Minerals*, 27, 327–338.
- Farfan, G.A., and Post, J.E. (2019) Quartz from Madagascar with fuchsinite phantom inclusions. *The Journal of Gemmology*, 36, 698–699.
- Farsang, S., Faq, S., and Redfern, S.A.T. (2018) Raman modes of carbonate minerals as pressure and temperature gauges up to 6 GPa and 500 °C. *American Mineralogist*, 103, 1988–1998.
- Fodor, M.A., Ható, Z., Kristóf, T., and Pósfai, M. (2020) The role of clay surfaces in the heterogeneous nucleation of calcite: Molecular dynamics simulations of cluster formation and attachment. *Chemical Geology*, 538, 119497.
- Gaál, L. (2008) Geodynamika a vývoj jaskýň Slovenského krasu—Geodynamics and development of caves in the Slovak Karst (in Slovak), 168 p. State Nature Conservancy of the Slovak Republic, Slovak Caves Administration, Žilina.
- Galindo-Gonzalez, C., Feinberg, J.M., Kasama, T., Gontard, L.C., Pósfai, M., Kósa, I., Duran, J.D.G., Gil, J.E., Harrison, R.J., and Dunin-Borkowski, R.E. (2009) Magnetic and microscopic characterization of magnetite nanoparticles adhered to clay surfaces. *American Mineralogist*, 94, 1120–1129.
- Gornitz, V. (1981) Phantom crystals. In *Mineralogy. Encyclopedia of Earth Science*, p. 368–369, Springer.
- Green, D.C., Ihli, J., Thornton, P.D., Holden, M.A., Marzec, B., Kim, Y.-Y., Kulak, A.N., Levenstein, M.A., Tang, C., Lynch, C., and others (2016) 3D visualization of additive occlusion and tunable full-spectrum fluorescence in calcite. *Nature Communications*, 7, 13524–13513.
- Haas, J., Demény, A., Hips, K., and Vennemann, T.W. (2006) Carbon isotope excursions and microfacies changes in marine Permian-Triassic boundary sections in Hungary. *Palaeogeography, Palaeoclimatology, Palaeoecology*, 237, 160–181.
- Hyodo, M., Sano, T., Matsumoto, M., Seto, Y., Bradák, B., Suzuki, K., Fukuda, J., Shi, M., and Yang, T. (2020) Nanosized authigenic magnetite and hematite particles in mature-paleosol phyllosilicates: New evidence for a magnetic enhancement mechanism in loess sequences of China. *Journal of Geophysical Research: Solid Earth*, 125, e2019JB018705.
- Johnston, W.D., and Butler, R.D. (1946) Quartz crystal in Brazil. *Bulletin of the Geological Society of America*, 57, 601–650.
- Kahl, C.F. (1965) Possible roles of clay minerals in the formation of dolomite. *SEPM Journal of Sedimentary Research*, 35, 448–453.
- Katz, B., Elmore, R.D., and Engel, M.H. (1998) Authigenesis of magnetite in organic-rich sediment next to a dike: Implications for thermoviscous and chemical remagnetizations. *Earth and Planetary Science Letters*, 163, 221–234.
- Katz, B., Elmore, R.D., Cogoini, M., Engel, M.H., and Ferry, S. (2000) Associations between burial diagenesis of smectite, chemical remagnetization, and magnetite authigenesis in the Vocontian trough, SE France. *Journal of Geophysical Research: Solid Earth*, 105, 851–868.
- Kim, Y.-Y., Ganesan, K., Yang, P., Kulak, A.N., Borukhin, S., Pechook, S., Ribeiro, L., Kröger, R., Eichhorn, S.J., Armes, S.P., and others (2011) An artificial biomineral formed by incorporation of copolymer micelles in calcite crystals. *Nature Materials*, 10, 890–896.
- Krishnamurti, D. (1957) The Raman spectrum of calcite and its interpretation. *Proceedings of the Indian Academy of Sciences—Section A*, 46, 183–202.
- Krishnan, R.S. (1945) Raman spectra of the second order in crystals Part I: Calcite. *Proceedings of the Indian Academy of Sciences—Section A*, 22, 182–192.
- Kulak, A.N., Semsarilar, M., Kim, Y.-Y., Ihli, J., Fielding, L.A., Céspedes, O., Armes, S.P., and Meldrum, F.C. (2014) One-pot synthesis of an inorganic heterostructure: uniform occlusion of magnetite nanoparticles within calcite single crystals. *Chemical Science*, 5, 738–743.
- Liu, D., Xu, Y., Papineau, D., Yu, N., Fan, Q., Qiu, X., and Wang, H. (2019) Experimental evidence for abiotic formation of low-temperature proto-dolomite facilitated by clay minerals. *Geochimica et Cosmochimica Acta*, 247, 83–95.
- Massey, M.J., Baier, U., Merlin, R., and Weber, W.H. (1990) Effects of pressure and isotopic substitution on the Raman spectrum of α -Fe₂O₃: Identification of two-magnon scattering. *Physical Review B, Condensed Matter*, 41, 7822–7827.
- McCarty, K.F., and Boehme, D.R. (1989) A Raman study of the systems Fe_{3-x}Cr_xO₄ and Fe_{2-x}Cr_xO₃. *Journal of Solid State Chemistry*, 79, 19–27.
- McCrea, J.M. (1950) On the isotopic chemistry of carbonates and a paleotemperature scale. *The Journal of Chemical Physics*, 18, 849–857.
- McHargue, T.R., and Price, R.C. (1982) Dolomite from clay in argillaceous or shale-associated marine carbonates. *Journal of Sedimentary Petrology*, 52, 873–886.
- Molnár, Z., Pekker, P., Dódy, I., and Pósfai, M. (2021) Clay minerals affect calcium (magnesium) carbonate precipitation and aging. *Earth and Planetary Science Letters*, 567, 116971.
- Montgomery, P., Hailwood, E.A., Gale, A.S., and Burnett, J.A. (1998) The magnetostratigraphy of Coniacian-Late Campanian chalk sequences in southern England. *Earth and Planetary Science Letters*, 156, 209–224.
- Németh, T., Máthé, Z., Pekker, P., Dódy, I., Kovács-Kis, V., Sipos, P., Cora, I., and Kovács, I. (2016) Clay mineralogy of the Boda Claystone Formation (Mecsek Mts., SW Hungary). *Open Geosciences*, 8, 259–274.
- Nyirő-Kósa, I., Rostási, A., Bereczk-Tompa, É., Cora, I., Koblar, M., Kovács, A., and Pósfai, M. (2018) Nucleation and growth of Mg-bearing calcite in a shallow, calcareous lake. *Earth and Planetary Science Letters*, 496, 20–28.
- Rae Cho, K., Kim, Y.-Y., Yang, P., Cai, W., Pan, H., Kulak, A.N., Lau, J.L., Kulshreshtha, P., Armes, S.P., Meldrum, F.C., and others (2016) Direct observation of mineral-organic composite formation reveals occlusion mechanism. *Nature Communications*, 7, 10187–10187.
- Ramamurthy, V., and Eaton, D.F. (1994) Perspectives on solid-state host-guest assemblies. *Chemistry of Materials*, 6, 1128–1136.
- Raub, T.D., Evans, D.A.D., and Smirnov, A.V. (2007) Siliciclastic prelude to Elatina-Nuccaleena deglaciation: Lithostratigraphy and rock magnetism of the base of the Ediacaran system. *Geological Society Special Publication*, 286, 53–76.
- Rehtijärvi, P., and Kinnunen, K.A. (1979) Fluid and mineral inclusions and inclusion zones of cave calcite from Korsnäs mine, western Finland. *Bulletin of the Geological Society of Finland*, 51, 75–79.
- Saloman, E.B., and Sansonetti, C.J. (2004) Wavelengths, energy level classifications, and energy levels for the spectrum of neutral neon. *Journal of Physical and Chemical Reference Data*, 33, 1113–1158.
- Shim, S.-H., and Duffy, T.S. (2002) Raman spectroscopy of Fe₂O₃ to 62 GPa. *American Mineralogist*, 87, 318–326.
- Sinkankas, J. (1966) *Mineralogy: A First Course*. Van Nostrand Company.
- Tombác, E., and Szekeres, M. (2006) Surface charge heterogeneity of kaolinite in aqueous suspension in comparison with montmorillonite. *Applied Clay Science*, 34, 105–124.
- Wanas, H.A., and Sallam, E. (2016) Abiotically-formed, primary dolomite in the mid-Eocene lacustrine succession at Gebel El-Goza El-Hamra, NE Egypt: An approach to the role of smectitic clays. *Sedimentary Geology*, 343, 132–140.
- Weber, J.N. (1964) Carbon isotope ratios in dolostones: some implications concerning the genesis of secondary and “primary” dolostones. *Geochimica et Cosmochimica Acta*, 28, 1257–1265.
- Woods, S.D. (2002) Paleomagnetic dating of the smectite-to-illite conversion: Testing the hypothesis in Jurassic sedimentary rocks, Skye, Scotland. *Journal of Geophysical Research*, 107.
- Zhou, D., Abdel-Fattah, A.I., and Keller, A.A. (2012) Clay Particles destabilize engineered nanoparticles in aqueous environments. *Environmental Science & Technology*, 26, 7520–7526.

MANUSCRIPT RECEIVED FEBRUARY 20, 2020

MANUSCRIPT ACCEPTED JULY 7, 2021

MANUSCRIPT HANDLED BY ADAM F. WALLACE

Endnote:

¹Deposit item AM-22-77483, Online Materials. Deposit items are free to all readers and found on the MSA website, via the specific issue's Table of Contents (go to http://www.minsocam.org/MSA/AmMin/TOC/2022/Jul2022_data/Jul2022_data.html).